

Efficient N-body Realisations of axisymmetric Galaxies and Haloes

Christian M. Boily¹

Astronomisches Rechen Institut, Mönchhofstrasse 12-14, D-69120 Heidelberg

Pavel Kroupa²

Institut für Theoretische Physik und Astrophysik, Universitaet Kiel, D-24098 Kiel, Germany

Jorge Peñarrubia-Garrido³

Astronomisches Rechen Institut, Mönchhofstrasse 12-14, D-69120 Heidelberg

Abstract

We present an efficient method for building equilibrium multi-component galaxies with non-spherical haloes and bulges. The gist of our approach is to tailor the velocity ellipsoid directly to the geometry of the mass distribution. Thus we avoid computing the anisotropic velocity dispersions which leads to large savings in the cpu budget. The computational time of the algorithm for triaxial equilibria scales linearly with the number of particles, N . The approximate solution to the velocity field causes structural relaxation: tests with $N = 50,000$ show that fluctuations of the inertia tensor (not exceeding the 10% level) disappear within one half of a revolution at the half-mass radius. At later times equilibrium properties settle to values close to those sought from the initial conditions.

A disc component is then added as described by Hernquist (1993). Incorporating the above algorithm to his code BUILDGAL, test runs show that the stability of the disc against vertical heating is not substantially modified by using our method.

The code, MAGALIE, is made generally available¹.

Key words: Galaxies, dynamics; halo; dark matter; numerical: method

PACS: 95.35+d, 95.75.Pq, 98.52-b

¹ Email : cmb@ari.uni-heidelberg.de

² Email : pavel@astrophysik.uni-kiel.de

³ Email : jorpega@ari.uni-heidelberg.de

1 INTRODUCTION

The visible Milky Way and other disk galaxies may be contained in extended dark-matter haloes of largely unknown morphology. Spherical haloes are typically assumed, but there are indications that this matter component may be significantly flattened, or even triaxial (see Zaritsky 1998, Sackett 1999, Rusin & Tegmark 2000). An important indicator is the non-isotropic distribution of satellites around disc galaxies, or the Holmberg effect (see Holmberg 1969). This may be a result of dynamical friction of non-spherically symmetric dark haloes acting on the satellites (Peñarrubia, Boily & Kroupa 2000).

Equilibria of self-gravitating galaxies are achieved for a given distribution function (df) based on three integrals of the motion. This approach faces a difficulty in that only the first two classical integrals (total energy E and one component of angular momentum \mathbf{J}) are known, the final integral taking an assumed form (see e.g. Lupton, Gunn & Griffin 1987; Einsel & Spurzem 1999). A greater difficulty still is that galaxies are heterogeneous systems of several components, and hence are hardly represented adequately with a unique df . A self-consistent equilibrium may be constructed by resorting to numerical integration of the equations of motion. Barnes (1988) introduced an iterative scheme by which particles relax in a fixed potential representing a galaxy component. This component is then given a particle representation in near-equilibrium.

Hernquist (1990, 1993) has introduced a by-now standard scheme which solves moments of the collisionless Boltzmann equation using tailored distribution functions. Three-component galaxies so constructed have the advantage over the Barnes approach of closer agreement with the sought equilibrium. In practice his algorithm is highly efficient when embedding a galactic disc in spherical components. (Benchmarking examples will follow in subsequent sections.) However we have found that for the purpose of constructing axisymmetric (non-spherical) bulges and haloes, the scheme requires significantly more cpu-time, mainly because one must solve numerically for the components of the velocity dispersion locally in three directions. This introduces an N^2 scaling of the computational time. By contrast, in spherical symmetry the velocity dispersion is known immediately from a one-dimensional integral (cf. [17] below). The algorithm of Hernquist (1993) remains efficient for up to tens of thousand of particles, however the computational time becomes prohibitive for larger numbers. Given that particle numbers adequate to galactic systems by far out-stretch available computer power, algorithmic problems such as this require solutions.

In this contribution we by-pass the Boltzmann equations approach, by noting that galactic components follow a well-defined hierarchy of sizes and masses. This suggests a perturbative treatment of particle potentials from the largest scales, down. Equilibrium solutions to Boltzmann equations in spherical symmetry are first transformed to the desired morphology directly, by mapping the velocity ellipsoid to the density isocontours. We construct equilibrium multi-component axisymmetric galaxy models by perturbing the velocity field of individual components to account for the added background potential (or, embedding). The computational time required for the whole procedure scales with particle number as for spherically symmetric models. Thus multi-component axisymmetric equilibrium configurations with millions of halo particles are easily constructed. In the following Section we review the problem and motivate our approach. This is then implemented and tested using a grid code. Benchmarking and comparisons with Hernquist’s standard BUILDGAL follow. We conclude with suggestions for applications and further improvements.

2 METHOD

2.1 Scaling of Computational Time

Approximate solutions based on moments of the Jeans equations have proved useful when constructing equilibrium galaxies. Hernquist (1993) has introduced a scheme whereby equilibrium galaxy components are first constructed in isolation, then zipped together by adding the gravity of the other components in turn. The modified binding energy of individual particles is matched by a similar increase in kinetic energy to preserve the structure of each component.

The case when all components are spherically symmetric allows a simplification. Then the added binding energy is measured from the increase in mass inside a particle radius r . To add together two or more spherical components only requires to sort the particles radially. The computational time required by a scheme such as QUICKSORT scales no faster than the 3/2-power of particle number (see e.g. Press et al. 1992, §8).

For non-spherical potentials however, the modified velocity field (and square velocity dispersions) requires the computation of the local potential (and its spatial derivatives) for each particle. The exact, direct-summation algorithm to do this requires a number of operations increasing in proportion to $\propto N^2$, the square particle number. The particle realisation of the density itself requires $\propto N$ operations. Thus in general we may write the total computational time to realise a compound equilibrium of c components as

$$T = \sum_{i=1}^c \left(\overbrace{N_i t_{den,i}}^{\text{Density}} + \underbrace{N_i t_{vel,i} \text{ or } N_i^2 t_{vel,i}}_{\text{Spherical or aspherical}} + \overbrace{N_i \sum_{j=1}^c N_j t_{cor,i}}^{\text{Background potentials}} \right) \quad (1)$$

where N_i is the number of particles for component i ; t_{den}, t_{vel} the computational times per particle to realise the density and velocity fields for respective components; and $t_{cor,i}$ the characteristic time for adjusting the velocity field of i^{th} -component particles due to non-spherical potentials. For three-component galaxies made of a spherical bulge (b), disc (d) and aspherical halo (h), we would write

$$T = N_h t_{den,h} + N_h^2 t_{vel,h} + N_h (N_d + N_b) t_{cor,h} + N_d t_{den,d} + N_d^2 t_{vel,d} + N_d (N_h + N_b) t_{cor,d} + N_b t_{den,b} + N_b t_{vel,b} + N_b (N_h + N_d) t_{cor,b} . \quad (2)$$

Clearly massive haloes call for large particle numbers and so the leading terms in (2) are $\propto N_h^2$ and $\propto N_h N_d$. We wish to remove these dependencies on N_h .

In any multi-component galaxy, the largest-scale structure would be closest to equilibrium self-gravity. This suggests that we look for a general scheme whereby the relative masses and scales of components are taken into account. Figure 1 provides a cartoon representation of our approach. Since details of the small scale components are lost on the much larger ones, a correction to the velocity field of larger structures would only involve truncated expansions of the small-component potentials. By contrast, a light structure requires more accurate treatment of the surrounding mass distribution: this is shown as light and heavy arrows on Fig. 1. We adopted this strategy by solving for the self-gravitating aspherical halo through a map of the velocity field of the spherical solution. As we shift down the scale ladder to smaller structures, higher-order expansions provide accurate corrections to the velocity field of individual components. Thus feedbacks from disc and bulge on the halo velocity field are given a low-order series-expansion treatment, while the velocity field of disc and bulge particles are adjusted with a high-order expansion of the halo potential. Below we take a stepwise angle to implementing this algorithm.

2.2 Self-gravitating axisymmetric equilibria

The basic step consists in building axisymmetric systems from a transformation of spherically symmetric equilibria. If we consider as given the geometric

aspect ratio and the mass profile of the equilibrium sought, it is then sufficient to construct a velocity field to match the gravity. In cylindrical coordinates ($R = \sqrt{x^2 + y^2}, z, \theta$), the orbits of stars in an axisymmetric harmonic potential are recovered from integrating two decoupled equations of motion. In the case of a uniform oblate spheroid of density ρ , axes a, c ; $a > c$, eccentricity $e = \sqrt{1 - c^2/a^2}$, the potential inside the bounding volume is (Table 2-1 in Binney & Tremaine 1987, hereafter BT+87; Chandrasekhar 1969, §3)

$$\Phi_{sp}(R, z) = -\pi G\rho \left(I(e)a^2 - A_1(e)R^2 - A_3(e)z^2 \right) \quad (3)$$

with known algebraic expressions for I, A_i . The motion of a test particle is found from solving for

$$\ddot{x}_i = -\nabla_i \Phi = -2\pi G\rho A_i x_i, \quad i = 1 \dots 3 \quad (4)$$

which admits a periodic solution in each component. Averaging the square velocity and position over one cycle, and substituting for A_i from Table 2.2 of BT+87, we obtain

$$\frac{\langle v_3^2 \rangle}{\langle v_1^2 \rangle} = \frac{A_3 \langle x_3^2 \rangle}{A_1 \langle x_1^2 \rangle} = \frac{A_3}{A_1} (1 - e^2) = 2 \frac{a/c - \sin^{-1}(e)/e}{\sin^{-1}(e)/e - c/a} \frac{c^2}{a^2}. \quad (5)$$

From (3) we find lines of constant potential intersecting the $z = 0$ plane and the z -axis such that for these coordinates $A_1 x_1^2 = A_3 x_3^2$. Defining the eccentricity of isopotential contours

$$e_\Phi \equiv \sqrt{\left(1 - \frac{x_3^2}{x_1^2}\right)_\Phi} = \sqrt{1 - \frac{A_1}{A_3}} \quad (6)$$

we may relate e_Φ to the geometric eccentricity (e) and that of the velocity ellipsoid, e_v , using (5) and (6)

$$e_v \equiv \sqrt{1 - \frac{\langle v_3^2 \rangle}{\langle v_1^2 \rangle}} = \left[\frac{e^2 - e_\Phi^2}{1 - e_\Phi^2} \right]^{\frac{1}{2}}. \quad (7)$$

The three quantities satisfy $e_\Phi < e_v < e$, and hence the velocity ellipsoid is never as flat as the mass distribution that gives rise to it. This result may be

derived directly from the virial theorem applied to the system as a whole (see BT+87, §4.3). Therefore, for the harmonic potential, (7) applies equally to averaged quantities and individual orbits.

In practice galaxies and haloes show peaked density profiles and hence the exact result (7) has limited application. An alternative to (7) is obtained by considering a star on a loop orbit in the mean potential of all the others. Since the matter is concentrated around the centre of gravity, a series expansion will be adequate when the orbit avoids the central region. Consider therefore the potential exterior to a homogeneous spheroid, of axes (a, c) equal to the mass-weighted means of the peaked distribution. This is written in a form analogous to (3) (BT+87, Chandrasekhar 1969),

$$\Phi_{sp}(R, z) = -\pi G\rho \frac{a^2 c}{(a')^2 c'} \left(I(a', c')(a')^2 - \sum_i A_i(a', c') x_i^2 \right). \quad (8)$$

In terms of (a, c) we have

$$\frac{R^2}{(a')^2} + \frac{z^2}{(c')^2} = 1; \quad a' \equiv \sqrt{a^2 + \lambda}, \quad c' \equiv \sqrt{c^2 + \lambda}. \quad (9)$$

For oblate spheroids the solution $\lambda(a, c, r)$ is expressed in algebraic form:

$$2\lambda = r^2 - a^2(2 - e^2) + \sqrt{(a^2 - c^2)^2 + 2a^2 e^2(z^2 - R^2) + r^4},$$

where $r^2 = R^2 + z^2$. (A relation similar to this one also exists for prolate spheroids but is omitted for reasons of clarity.) The solution $\lambda > 0$ applies outside the bounding surface of the spheroid. For a loop orbit with $r > a$ a series expansion of (8) leads to (cf. Goldstein 1980, eq. 5-88)

$$\Phi_{sp}(R, z) = -\frac{GM_o}{r} + \frac{GM_o}{2r^3}(I_z - I_R)P_2(\cos \theta) + O([a/r]^4) \quad (10)$$

where $\tan \theta = z/R$, $P_n(x)$ is a Legendre polynomial, and I_x an eigen-component of the inertia tensor per unit mass and we consider only the half-space $z > 0$ in what follows. Integrating the equations of motion for the potential (10) leads to solutions of the form

$$x_i(t) = x_{o,i} \cos[w_1(t - t_o)] \left(1 + \frac{w_2^2 x_{o,i}^2}{w_1^2 8r^2} \cos^2[w_1(t - t_o)] + \dots \right) \quad (11)$$

where

$$w_1^2 = G\bar{\rho} + \frac{9}{2}G\bar{\rho} \frac{I_z - I_R}{r^2} ; w_2^2 = \frac{9}{2}G\bar{\rho} \frac{I_z - I_R}{r^2} ; \bar{\rho} \equiv \frac{M}{4\pi r^3/3} .$$

Thus when $r \gg a > c$, $w_2 \rightarrow 0$ with $1/r^2$ since the I_i 's are constants. The orbits describe ellipses of the same eccentricity in both $\dot{\mathbf{x}}$ and \mathbf{x} . Note when $I_z = I_R$, (11) reduces to solutions for the right-hand side in (4). For such orbits we would therefore set

$$e_v = e . \quad (12)$$

Our solutions (7) and (12) bracket the range of possible aspect ratios the velocity ellipsoid may assume in equilibrium. Realistic galaxy equilibria will fall somewhere between strict homogeneity and point-mass distributions. We therefore sought a sensible interpolation for e_v in the range e_Φ to e to account for this. The number of possibilities is *a priori* endless. We chose for each particle i

$$e_{v,i}^2 = e_\Phi^2 + (e^2 - e_\Phi^2) \sqrt{1 - \frac{\langle r^2 \rangle}{r_{g,i}^2}} \quad (13)$$

which was found to yield adequate equilibria. In computing e_v , we substitute in the above the mass-weighted average r^2 inside the spherical volume $4\pi r_{g,i}^3/3$. To obtain an eccentricity for the velocity ellipsoid that reflects the character of the gravitational field sampled by the star over one orbit, we compute the gravitational radius

$$r_{g,i} = \frac{GM}{-E_i} ,$$

where E_i is the binding energy of the i^{th} star, and M the total mass of the system. The velocity ellipsoid computed from (13) is the same for all stars of the same binding energy. We give some motivation for the interpolation (13) through an example.

To fix ideas, consider a Dehnen model for spherical galaxies. Dehnen (1993) introduced a family of potential-density pairs which provide a suitable fit to bulges and cuspy ellipticals :

$$M(r) = M_o \left(\frac{r}{r+r_c} \right)^{3-\gamma} ,$$

$$\Phi(r) = \frac{GM_o}{r_c} \times \begin{cases} \frac{1}{2-\gamma} \left(1 - \left[\frac{r}{r+r_c} \right]^{2-\gamma} \right) & (\gamma \neq 2) \\ \ln \frac{r}{r+r_c} & (\gamma = 2) \end{cases} . \quad (14)$$

Here (r_c, γ) are two parameters and the total system mass = M_o . The case $\gamma = 1$ corresponds to a spherical Hernquist (1990) density profile. Let $r_c = 1/10$, and we truncate the distribution at $r = 1$ for convenience. With $M_o = 1.21..$ the mean square radius $\langle r^2 \rangle = 0.349...$, enclosing 63% of the mass. We invoke the virial theorem and set $E_i = -\Phi_i/2$ for a given stellar orbit. Using this in (14) we compute $r_{g,i} = GM_o/(-\Phi_i/2) = 2(r_i+r_c)$; the ratio of averaged values $\langle r_g \rangle / \langle r \rangle = 1/4$. If we now squash the sphere down the z-axis to achieve an aspect ratio $c/a = 1/2$, we compute from (13) an eccentricity $e_v \approx 0.860..$, close to $e = \sqrt{1 - c^2/a^2} = 0.866...$ Setting $\gamma = 0$ so that the central region is of uniform density, we find from (7) for this model $e_v = 0.832..$, nearly unchanged from the previous value. This is because only $\approx 12\%$ of the mass now resides inside $r = r_c$. Thus unless the galaxy shows a broad uniform density region, the solution (13) on the mean lies close to e .

3 Stand-alone Axisymmetric Haloes and Bulges

We now implement the scheme described above. We begin by summarising the steps used in constructing spherical equilibria. Applications will centre on the Dehnen models (14), as they cover a range of central density gradients (through the index γ) from which to test the method. We concentrate on two aspects, namely the stability of equilibria so constructed and the range of cases to which this algorithm may be applied. We consider isolated self-gravitating haloes first; multi-component models are discussed in the next section.

3.1 Spherically Symmetric Equilibria

For the case of spherically symmetric mass profiles the potential at radius r is

$$\Phi(r) = - \int_{\infty}^r \frac{GM(x)}{x^2} dx = - \int_{\infty}^r G \frac{dx}{x^2} \int_0^x 4\pi u^2 \rho(u) du \quad (15)$$

provided the run of mass $M(r)$ increases more slowly than $\propto r$ at large distances. The mass distribution is a given quantity of the problem. A particle representation of any mass profile $M(r)$ can be obtained straightforwardly, first by filling a spherical volume uniformly by Monte Carlo method, then mapping the mass shells to the desired profile, i.e. $M_h(\hat{r}) = M(r)$, with M_h the uniform-density spherical profile. The solution $r(M)$ is not known in analytic form in general and must be tuned by interpolation when only a discrete representation $M_i(r_i)$ is given on input. One advantage over solving directly by Monte Carlo method for $r(M)$ is that a unique realisation $M_h(\hat{r})$ may be transformed to a variety of profiles. This essentially keeps any bias due to \sqrt{N} fluctuations the same for different $M(r)$. This is especially important in systems where the effect of low- N statistics may be felt, such as in central galactic cusps. Interpolation errors would wipe out this advantage when the desired mass profile is known only on a coarse mesh $\{r_i\}$.

The problem is complete once the velocity field satisfying the Jeans equations under $\Phi(r)$ is solved for. From the first of these equations (cf. Binney & Tremaine 1987, §4.2),

$$\frac{d\rho\overline{v_r^2}}{dr} + \frac{\rho}{r} [2\overline{v_r^2} - \overline{v_\theta^2} - \overline{v_\phi^2}] = -\rho \frac{d\Phi}{dr}, \quad (16)$$

for an isotropic velocity field the solution takes the form

$$\overline{v_r^2} = \frac{-1}{\rho(r)} \int_r^\infty \rho(x) \frac{d\Phi}{dx} dx = \frac{1}{\rho(r)} \int_r^\infty \rho(x) \frac{GM(x)}{x^2} dx. \quad (17)$$

With a known velocity dispersion at each radius it is customary to seek closure by picking a form for the velocity $d\mathbf{f}$. We will assume a velocity dispersion taking locally a Maxwellian form (Hernquist 1993),

$$F_v(\mathbf{v}, r) d^3\mathbf{v} = 4\pi \left(\frac{1}{2\pi\sigma^2} \right)^{\frac{3}{2}} v^2 \exp(-v^2/2\overline{v_r^2}) dv. \quad (18)$$

N-body realisations of a Maxwellian distribution would require integrating to infinity in velocity space. In practice bound particles all have velocities below the local escape velocity ($= \sqrt{-2\Phi(r)}$), effectively setting an upper-limit for v

in (18). A proper implementation of this renormalises the velocities to preserve the Maxwellian character of the field, so

$$\overline{v^2}(r) = 3 \sigma^2(r) , \quad (19)$$

where σ is the one-dimensional velocity dispersion at r and $\sigma^2 = \overline{v_r^2}$ for non-rotating distributions.

3.2 From spheres to axisymmetry

To construct axisymmetric halo and bulge components, we proceeded as follows. Our starting point is a spherical equilibrium constructed as in the above. With $M(r)$ known, the potential $\Phi(r)$ and velocity dispersion are evaluated for member stars from (15) and (17). Each particle is then given a velocity drawn from the distribution (18). Since only one-dimensional integrals are involved, the computational requirements for this part of the calculation scales with $\propto N$, where N is the total number of particles.

We then perform a homologous transformation of the position of each particle to achieve the desired morphology. The case where isodensity contours are concentric oblate spheroids is a good starting point. The particles are then mapped according to $(x, y) \rightarrow (x, y)$, $z \rightarrow z\sqrt{1 - e^2}$. The quantities $\langle r^2 \rangle$ and r_g are computed directly from $M(r)$, prior to the mapping.

To modify the velocity field requires evaluating the potential energy of each particle in the new spheroidal potential, $\Phi_{sp}(R, z)$. The quantity $\sqrt{\langle r^2 \rangle}$ is computed from mass lying inside any particle radius, r , for which we define a uniform density spheroid of axes $(\sqrt{\langle r^2 \rangle}, \sqrt{\langle r^2 \rangle}\sqrt{1 - e^2})$, total mass $M(r)$. Equations (8) and (9) then yield the correct potential at (R, z) up to quadrupolar order. By virtue of the virial theorem half of the potential energy accrued by the stars through the coordinate transformation should be invested in kinetic energy. Thus

$$T_i = E_i - \Phi(r_i) \rightarrow T'_i = T_i + \frac{\Phi(r_i) - \Phi_{sp}(R_i, z_i)}{2} \quad (20)$$

for each particle i . The velocity vector \mathbf{v}'_i must satisfy (13), which is the case when

$$\mathbf{v}'_i = \sqrt{\frac{2T'_i}{2T_i - v_z^2 e_v^2}} \times (v_x, v_y, v_z \sqrt{1 - e_v^2}) .$$

In the above the primed quantities refer to the transformed, final state. The multiplicative factor ensures the new velocity gives the kinetic energy (20). The new potential could have been evaluated from (10), by computing the inertia tensor inside the spheroid $(r, r\sqrt{1 - e^2})$, for each particle. However (9) and (8) require only evaluating trigonometric functions and the algorithm is therefore optimised for the transformation we have performed here. When the eccentricity of the isodensity contours vary with position, one requires averaged eccentricities in (13) for every mass shell, which is provided through (10) by the tensor of inertia.

3.3 Numerical Setup

The algorithm we have described was tested using the nested-grid integrator SUPERBOX (Fellhauer et al. 2000). The tests we conducted used in total $N = 50000$ particles. Since spherical equilibria provide the work horse of the scheme, we first constructed a spherical equilibrium to tune up the code.

The spherical profile used is the Dehnen family (14) with $\gamma = 1$ and $a = 1/10$. The models were all truncated at $R_{cut} = 1$. We then evolved the distributions for 3 to 4 circular orbits at the half-mass radius, each revolution corresponding to time intervals $4t_{cr} = 4\sqrt{3\pi/16(G\bar{\rho})^{-1}}$, where t_{cr} is the dynamical time and $\bar{\rho}$ the averaged density at the half-mass radius. Setting $G = 2$ we have $4t_{cr} = 0.727..$ for a single revolution about the half-mass volume. At the edge of the system an orbit takes $\simeq 2.05..$ units of time for a revolution.

SUPERBOX is a time-centred leap-frog integrator. The timestep we selected $= 0.006 \times t_{cr}$; the radius where this timestep matches the local dynamical time for an Dehnen $\gamma = 1$ model is at (roughly) $1 \times 10^{-3} \times a$, enclosing $\sim 10^{-4}$ percent of the mass. The dynamics is therefore well resolved in time for all particles in the simulations. In general the central cusp is poorly resolved by grid codes due to finite linear resolution. However the three levels of resolution allowed by SUPERBOX means that we can focus on the central region and boost resolution as needed. Setting the total grid size $= 1/2$ we then find for an 32-mesh grid a linear resolution $l \approx 1/2 \times 1/32 = 0.016$ such that 2 percent of the total mass falls inside the innermost grid points. This would minimise structural evolution, however the coarse central density due to finite resolution means that velocity field and potential no longer match there, resulting in a small degree of relaxation at the centre.

The left-hand panels on Fig.2 show the results of evolving a spherical Dehnen $\gamma = 1$ model. The figure displays the 10-percentile Lagrange radii of the mass sorted in spherical shells. We note that systematic fluctuations are low for the innermost mass shells. However near the edge appreciable evolution can be seen, at a level of 15% for the 90% mass radius. Bearing in mind this caveat, we then applied the same numerical setup to flattened Dehnen models. To preserve the good resolution of the dynamics in time, we enforced identical central density for all models by an homologous transformation of the particle positions, so the dynamical time t_{cr} remains the same.

3.4 Results for axisymmetric models with $\gamma = 1$

Non-rotating self-gravitating equilibria of aspect ratios $c/a > 1/3$ are susceptible to bending modes of instability (Combes et al. 1990, Sellwood & Wilkinson 1993). No elliptical galaxy has a projected aspect ratio flatter than E7 (Binney & Merrifield 1998). Furthermore the narrow stream of debris from the Sagittarius dwarf suggests that the halo of the Milky Way may be as round as or rounder than E1 (Ibata & Lewis 1998). Therefore we consider a flattened model with $c : a = 1 : 3$ as a limiting case to test the algorithm. This is done first, before investigating the effects of varying aspect ratio and power index γ .

Figure2(b) graphs the Lagrange radii of an 1:3 flattened Dehnen model. The mass profile has been binned in spherical shells to facilitate comparisons with the spherical case. Assessing the overall setup, we find as expected a degree of relaxation in the innermost mass bins. Close inspection shows fluctuations of amplitude ~ 0.01 forming at all Lagrange radii. These fluctuations propagate inside out, and result from stars leaving the central region. For the model at hand we estimate that 2.8% of the total mass gives rise to them. At the end of this simulation only 0.52% of stars had left the volume of the simulation, therefore we conclude from this exercise that $\approx 2\%$ of kinetic energy is not assigned correctly by our application of (20) and leads to large errors in the binding energy of relatively few particles.

We monitor in time the morphology of the model defining the mass-weighted principal axes

$$a_i^2 \equiv \frac{I_j + I_k - I_i}{2} \quad (21)$$

where $\{I_i\}$ are the eigenvalues of the inertia tensor and $\{i, j, k\} = \{x, y, z\}$ and permutations thereof (Goldstein 1980, §5-3; see also Kroupa 1997). Particles are first selected in spherical Lagrangian shells, from which the I_i 's are

computed. A first estimate of the principal axes of the mass distribution is computed from (21). A second selection of particles is then made, with the bounding volume now assuming the ellipsoidal shape defined by the a_i 's. The inertia tensor and eigenvalues are recomputed from this new selection to obtain the final estimate of the system axes. Figure 3 (left-hand panel) graphs the evolution of the quantity $2a_3/(a_1+a_2)$ for two mass bins, the 30% and 60% Lagrange radii. For clarity the 30% results were divided by a factor two. We find the relaxed configuration giving nearly the exact same quantities after a half-unit of evolution. It is noteworthy that relaxation was more severe in the central region, where the computed aspect ratio drops from 0.18 initially to 0.16 at later times. The right-hand panel shows the velocity field for the 60% innermost particles. Here there are virtually no signs of evolution or trends beyond the level of root- N fluctuations.

3.5 Models with $\gamma \neq 1$

We investigated the range of applicability of our approach by evolving Dehnen models with different power indices γ . The solution (7) for the velocity ellipsoid applies to harmonic potentials of uniform density. Since we opted instead to implement (13), we ask whether equilibria can be setup this way with a harmonic central core, i.e. for models with $\gamma = 0$.

Figure 4 (left-hand panel) illustrates the impact of the central harmonic core. We have graphed the same quantities as on Fig. 3, using the same numerical setup to validate the comparison. The oscillations of the 60% axis ratio seen early on in the simulation compare in magnitude to those observed for the $\gamma = 1$ case. However in the inner region the ratio varies from 0.18 initially, to 0.15 after one time unit of evolution, or down 17%, somewhat more than what was observed for the same volume in the case of $\gamma = 1$, where variations were of $\simeq 11\%$ relative magnitude.

The multipolar expansion of the gravitational field suffers less from truncation if the matter is more concentrated about the centre of gravity. Therefore Jaffe's (1983) profiles (Dehnen $\gamma = 2$) provide another test since they are more concentrated. The right-hand panels on Fig. 4 show indeed that fluctuations due to dynamical relaxation are much reduced for the period $t < 1/2$. The principal axes ratio fluctuates between 0.17 ± 0.01 or 5.9% for the inner 30% mass radius. At larger volume it fluctuates initially by a similar relative fraction. We would expect this property to prove helpful when modelling dark haloes as isothermal gas, for which asymptotically $\rho \propto r^{-2}$ at large distances.

4 Multi-component Models

The map (13) provides equilibria for one-component self-gravitating spheroidal galaxies. We now generalise to multi-component galaxies. Our goal is to verify that the embedding of new components does not introduce further evolution in the structure of the galaxy. In an effort to bring out algorithmic, as opposed to dynamical, biases, we have put together a bulge-disc-halo model galaxy where the bulge and halo have the same spherical Dehnen $\gamma = 1$ mass profiles. We then opted to combine a spherical bulge, exponential disc and axisymmetric halo, requiring respectively zero-, high- and low-order corrections to the monopole for a precise determination of the potentials. We modified a version of BUILDGAL kindly provided to us by L. Hernquist and based on his 1993 algorithm. We implemented the map of Section 2.2 for axisymmetric galactic potentials, taking into account the hierarchy of individual components.

4.1 *Disc, bulge & halo galaxy*

While not attempting to model the Galaxy, we set up model galaxies with relative masses and lengths in rough agreement with those of Freudenreich (1998) for the Milky Way (see Sackett 1997, Binney & Merrifield 1999, §10). In model units, the bulge has a mass and radius = 1; the core length $r_c = 0.10$. The exponential disc has a radial scale length $h = 1.0$, scale height $z_o = 0.3$, total radius = 10 and mass = 3.0. We chose scale lengths h and z_o large compared with the linear resolution $l = 0.016$ in the inner region of our grid code.

The heavier spheroidal halo was given an 1:2 aspect ratio as described in Section 2.2. We took z as the symmetry axis so the spheroid equator lies in the x-y plane. The halo has a total radius = 20.00, mass = 30.00, and we chose a halo core length $r_c = 2.0$. The halo and disc masses are in the ratio 4:1 at the edge of the disc, so the halo drives the dynamics there but not overwhelmingly so. This is done on purpose, with a view to perturb the halo equilibrium, as it must adjust to the disc gravity.

4.2 *Computing the potentials*

Experience and pragmatic considerations led to the following simplifying tricks. When computing the disc feedback on embedded bulge particles, we have kept the direct-summation algorithm from the original code, since the dimensions of the bulge are comparable to the disc scale length. Hence a multipole expansion would require high-order series expansion which we deemed not essential, as

the number of bulge particles is less or comparable to the number of disc particles, which already gives $t \propto N_d^2$ scaling of computational time (cf. equation 2). We found the direct-summation computation, contributing a term $\propto N_d N_b$ in the total computational time, gives better result than a expanding the disc potential to high-order, although a crude evaluation using (8) also provides a sensible equilibrium - see below. The feed-back of the bulge on disc particles however is accounted for already when the monopole term of its potential is added to that of the disc.

The halo and disc interactions require some care. We found it sufficient for an axisymmetric halo to expand its potential to quadrupolar term (cf. [10]) and adding this to the disc's (and the bulge's) self-gravitating potentials. Equation (10) is easily differentiated in three dimensions. The kinetic energy is then added to the disc and bulge particles for each degree of freedom in the same proportion as the components of the halo gravitational forces (to account for the work done in reshaping the system). In this way, relatively more kinetic energy is invested in the x-y plane, when compared with the z-direction, to fight off the enhanced gravity due to the flattened halo in the equatorial plane of the spheroid. As the rms disc aspect ratio is close to 1:12, the boost in disc kinetic energy required to maintain equilibrium was added to the circular motion at cylindrical radius R for each disc particle. Since the streaming motion at R is known, energy can be directly added to each particle once (20) has been computed.

As halo particles spend little time near or in the plane of the disc, we treated the disc as a highly flattened oblate spheroid, for which the potential is computed from (8). To do so we averaged over the vertical structure of the disc, however the original scales of height and radial decay are preserved if we use as spheroid axes the mass-weighted disc parameters $\langle R \rangle$ and $\langle z \rangle$. This effectively removes the term $\propto N_d N_h$ of the total computational time (2).

4.3 Results

For comparison purposes we display two models on Fig. 5. The first one has both spherical bulge and halo, while the second has an oblate spheroidal halo of aspect ratio 1:2. The motivation for doing this is clear: for spherically symmetric components, the multipole approach becomes exact, since only the monopole term contributes to the potential of each component. Models of a disc galaxy with spherical bulge and halo thus minimise relaxation effects.

The structure of the bulge is well accounted for by sorting the mass on spherical Lagrangian shells. For the case of the disc, of mean aspect ratio $\simeq 1 : 12$, the Lagrangian shells effectively follow the cylindrical radii. Contrasting the

two models, with and without spherically symmetric halo, we find little effect on the radial structure of disc and bulge introduced by our approximate treatment. In both the cases, radial oscillations are seen to propagate from the inside, outwards, while taking several dynamical times to dampen. On the figure the arrows indicate the dynamical time t_{cr} at the half-mass radius (bulge and halo) or at $R = h$ (disc) of individual components in isolation. These radial oscillations give rise to transient patterns on visual inspection. We note that after a few revolutions of the disc at $R = h$, much of the fluctuations have disappeared or are much attenuated.

The moments of inertia give insight into the structure of individual galaxy components. On Fig. 6 we display the moments of inertia, principal axes and velocity dispersion components of the bulge and halo for the case where the halo is an oblate spheroid. We find as on Fig. 2 slight changes in the ratio of principal axes of the halo. However, after settling, the structure remains close to the one specified on input. The bulge, on the other hand, is clearly stretched out of spherical symmetry, due to the combined pull of the disc and halo: at the edge of the bulge, $R = 1$, the halo mass $\approx 10/3$ is already several times that of the bulge, which is not fully self-gravitating anymore. The aspect ratio of the bulge in equilibrium is close to $0.65/0.75 = 0.87$, when we would want unity. The external forces acting on the bulge leads to expansion, as seen from the increased moments of inertia (top left-hand side panel). A quick solution to counter this effect would be to stretch the bulge initially to mildly prolate structure of axis ratio $a : c \sim 1 : 1.1$, so as to relax to near sphericity. We have not resorted to this therapy and chose instead to illustrate the limitations of the algorithm.

Turning to the vertical structure of the disc, we averaged the height $|z|$ of stars inside $R = 2h$, since this region is well resolved by our grid code and errors due to numerical integration are reduced. We computed both average vertical height and the one-dimensional velocity dispersion σ_z for ten snapshots covering ten time units of evolution, or four revolutions. Table 1 gives the results. Early in the evolution of the disc, the vertical structure shrunk by $\approx 15\%$, as the mean height drops from ≈ 0.2 to ≈ 0.17 . We observed a decrease of the standard deviation as well, of the same magnitude, which leads us to conclude in a global contraction of the vertical disc structure. This is matched by a rise in velocity dispersion of the same relative magnitude (see Table 1). Since $\langle v_z \rangle \approx 0$ and is much less than the vertical velocity dispersion, the bulk motion remains negligible throughout.

4.4 Benchmarks

Approximate methods such as the one we have presented would not be of interest without a handsome pay-out at the computer. We find the scaling properties of the method with a series of numerical tests. Specifically, we first bench-marked the original version of the code BUILDGAL for spherical bulge + disc galaxy models. We then constructed an axisymmetric bulge using the full algorithm, which computes the response of the disc to bulge potential exactly. Since bulge and halo are constructed in the same way in BUILDGAL, and the disc embedding done in the same exact fashion, we may relabel the bulge as halo. This is so when referring to BUILDGAL below. In a second set of tests, we repeated these experiments, using the new version of the code. The same default disc parameters were used in all our tests, and haloes were given Hernquist (1990) mass profiles with $r_c = 0.1$, and truncated at the disc edge.

All benchmarks refer to an 333 MHz G3 Apple processor operating under S.u.S.E. Linux 6.4 OS; we compiled BUILDGAL with the widely available GNU Fortran compiler G77 -O4. The performance were done with disc and bulge particle numbers, N_d, N_b , in the range 5,000 to 5×10^4 (disc); and 5000 to $N_b = 5 \times 10^5$ (bulge or halo).

We solved for the operation times $t_{x,i}$ in (2), first as a set of linear equations by constructing stand-alone disc and bulge (no feedback terms present), then re-doing the calculations with disc and bulge together. Our results are listed in Tables 2 and 3. The most important point to notice is the large increase in computer time for models with an axisymmetric bulge, which scales effectively with the square of particle number. The turn-over to quadratic dependence is approximately 2×10^4 particles. The validity of (2) is inferred from the convergence of the operation times $t_{x,i}$'s with increasing N . We have extrapolated to infinite particle numbers using the polynomial fit routine PZEXTR of Press et al. (1992). The numbers are truncated to the last significant digit according to error estimates obtained from the results of the two highest-order polynomial fits.

Repeating this exercise with the new algorithm, we concentrated on the case of an axisymmetric halo + disc, since the case of a spherical halo would give essentially the same $t_{x,i}$'s. We therefore have to compute only the extra computational time required for the transformation of the halo to axisymmetry and its coupling with the disc. We find as expected that the time required to adjust the disc and halo velocity fields scale in proportion to their respective particle numbers. A comparison of total computational time shows that axisymmetric compound models require only a modest increase in computer time when compared with spherically symmetric components. The new code, MAGALIE (for Mache Galaxie), can thus construct galaxies with bulge, disc

and halo, all in axisymmetry, at virtually no extra costs.

5 CONCLUSIONS

We have presented a method of constructing approximate equilibria in good agreement with those sought. In particular the algorithm scales linearly with bulge and halo particle numbers, when these are axisymmetric or spherical. The approach takes into account implicitly the relative scales of components involved, and treats the interactions between components by expanding the potential to required order (Fig. 1).

The errors introduced from treating non-spherically symmetric components was found to be no worse than the case where only spherical components surround a disc. The required computational time for this algorithm scales with particle numbers as

$$t_{\text{cpu}} = N_h t_{\text{den},h} + N_h t_{\text{vel},h} + N_h t_{\text{cor},h} + N_d t_{\text{den},d} + N_d^2 t_{\text{vel},d} + N_d t_{\text{cor},d} \quad (22)$$

where the parameters $t_{x,i}$ are given in Table 3 for a G3 processor (see Section 4.4). With this algorithm non-spherical haloes surrounding galaxies can be constructed as a matter of routine. The results of a parameter survey of orbital decay in aspherical haloes will be presented in a separate contribution (Peñarrubia et al. 2000).

We have limited our discussion to prolate spheroidal potentials. The approach is readily applicable to prolate or triaxial structures however. To construct triaxial equilibria, one would map the axes of the velocity ellipsoid as in (13) to the geometry of the triaxial body. Equations (8) and (10) are easily generalised to triaxial systems (BT+87). Likewise, net rotation of individual components is implemented by alignment of particle angular momenta (see e.g. Lynden-Bell 1962, Hernquist 1993). Models of barred galaxies may possibly be constructed by converting random into bulk motion of a triaxial component, but we have not implemented this.

The disc self-gravity now represents the bottleneck through the N_d^2 term in equation (22). For situations where the disc substructure can be neglected, this dependence may be removed by constructing a disc from flattening a spheroid to small aspect ratio, then converting random motion to provide rotational support. When the disc structure matters to the dynamics however, this approach is unlikely to yield sensible disc equilibria, because the vertical and radial motions in thin structures require fine-tuning the velocities locally, hardly in line with such a brute-force approach. Note however that one may

construct a disc similar to the Milky Way's by considering the thin and thick discs as separate components. These may then be combined in the fashion described in Section 2. Sellwood & Wilkinson (1993) discuss methods of constructing stable thin galactic discs comprehensively.

Acknowledgements

CMB and JPG acknowledge support from the German government through an SFB 439 grant at the Karls-Ruprecht-Universität Heidelberg.

Note added in proof - After this article was submitted, we found a natural, quick-fix solution to the ' N_d^2 ' scaling of the thin disc construction algorithm (cf. Tables 2 and 3): it consists in adding together m realisations of an n -particle disc to reach the desired total particle number $N_d = m \times n$. The total cpu then scales with $m \times n^2 \sim n \times N_d$, or linearly with N_d . Though n and hence the coefficient of proportionality should be reasonably large to dampen numerical noise, the approach is well-suited to parallel algorithms.

References

- Barnes, J.E. 1988, ApJ, 331, 699
- Binney, J.J., & Merrifield, M. 1998, Galactic Astronomy (Princeton: University Press)
- Binney, J.J., Tremaine, S.D. 1987, Galactic Dynamics (Princeton: University Press)
- Chandrasekhar, S. 1969, Ellipsoidal Figures of Equilibrium (New York: Dover)
- Combes, F., Debbash, F., Friedli, D., et al. 1990, A&A, 233, 82
- Dehnen, W. 1993, MNRAS, 265, 250
- Einsel, Ch., & Spurzem, R. 1999, MNRAS, 302, 81
- Fellhauer, M., Kroupa, P., Baumgardt, H., et al. 2000, New Astronomy, 5, 305
- Freudenreich, H.T. 1998, ApJ, 492, 495
- Goldstein, H. 1980, Classical Mechanics (Singapore: Addison-Wesley)
- Hernquist, L. 1990, ApJ, 356, 359
- Hernquist, L. 1993, ApJS, 86, 389
- Holmberg, E. 1969, Arkiv Astr., 5, 305

- Ibata, R., & Lewis, G. 1998, *ApJ*, 500, 575
- Jaffe, W. 1983, *MNRAS*, 202, 995
- Kroupa, P. 1997, *New Astronomy*, 2, 139
- Lupton, R.H., Gunn, J.E. & Griffin, R.F. 1987, *AJ*, 93, 1114
- Lynden-Bell, D. 1962, *MNRAS*, 123, 447
- Peñarrubia, J., Boily, C.M., & Kroupa, P. 2000, in preparation
- Press, W.H., Teukolsky, S.A., Vetterling, W.T. et al. 1992, *Numerical Recipes* (Cambridge: University Press), 2nd edition
- Rusin, D., & Tegmark, M. 2000, [astro-ph/0008329](https://arxiv.org/abs/astro-ph/0008329)
- Sackett, P. D. 1997, *ApJ*, 483, 103
- Sackett, P. D. 1999, in *A.S.P. Conf. Series Vol. 182, Galaxy Dynamics*, ed. D. Merritt, J. Sellwood & M. Valluri (San Francisco: ASP), 393
- Sellwood, J., & Wilkinson, A. 1993, *Rep. Prog. Phys.*, 56, 173
- Zaritsky, D. 1998, (ed.) *Galactic Halos*, *A.S.P. Conf. Series Vol. 136* (San Francisco: ASP)

time	N	$\langle z \rangle$	δz	$\langle v_z \rangle$	σ_z^2
0	5921	0.207	0.176	-8.14×10^{-3}	0.912
1	5833	0.169	0.163	4.6×10^{-4}	1.084
2	6147	0.169	0.160	1.74×10^{-2}	1.032
3	5960	0.168	0.162	4.04×10^{-2}	1.061
4	5936	0.167	0.158	4.79×10^{-2}	1.072
5	6006	0.168	0.164	1.86×10^{-2}	1.070
6	5895	0.169	0.161	-4.5×10^{-4}	1.068
7	5975	0.171	0.165	4.09×10^{-2}	1.060
8	5895	0.170	0.158	8.44×10^{-2}	1.078
9	5930	0.173	0.163	8.47×10^{-3}	1.066
10	5973	0.170	0.159	4.29×10^{-2}	1.099

Table 1

Time-evolution of the vertical structure of an embedded disc in a flattened spheroid. Only particles inside cylindrical radius $R = 2h$, where h is the radial disc scale length, are included when computing mean height and velocity dispersion. The standard deviation $\delta z \equiv \sqrt{\langle (|z| - \langle |z| \rangle)^2 \rangle}$.

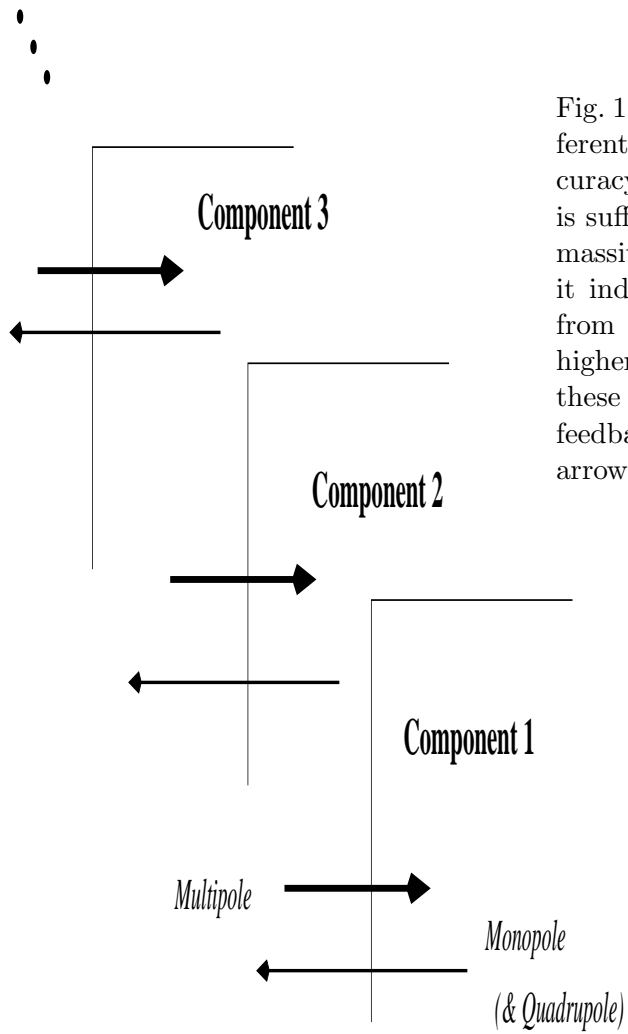


Fig. 1. Coupling galaxy components of different linear sizes and masses. A low accuracy treatment of the total potential is sufficient to maintain the largest, most massive component in equilibrium, while it induces a relatively stronger response from the smaller components, requiring higher-order treatment of the potential for these components. The strength of the feedback is shown here as light and heavy arrows.

$$(A) \text{ Total cpu} = N_h \times (t_{den,h} + t_{vel,h}) + 2 N_d N_h t_{cor,h} + N_d t_{den,d} + N_d^2 t_{vel,d}$$

N_h	$t_{den,h}$ [10^{-5} s]	$t_{vel,h}$ [10^{-5} s]	$t_{cor,h}$ [10^{-5} s]	N_d	$t_{den,d}$ [10^{-5} s]	$t_{vel,d}$ [10^{-5} s]	CPU [seconds]	
							True	Computed
$5 \cdot 10^3$	3.80	6.70	0.096	$5 \cdot 10^3$	27.2	0.368	141.9	83.7
10^4	3.90	6.10	0.092	$5 \cdot 10^3$	27.2	0.368	186.4	141.1
10^4			0.096	10^4	27.3	0.222	417.7	231.4
10^4			0.106	$2 \cdot 10^4$	27.4	0.159	1066.5	862.0
10^4	3.90	6.10	0.107	$5 \cdot 10^4$	27.3	0.112	3884.6	3653.9
$2 \cdot 10^4$	3.80	4.90	—	10^5	26.8	0.102	10228.5	10027.9
$5 \cdot 10^4$	3.80	4.10					3.95	3.64
10^5	3.80	3.80					7.60	7.28
$5 \cdot 10^5$	3.70	3.60					36.50	36.40
∞	3.64	3.54	0.114	∞	26.5	0.100		

$$(B) \text{ Total cpu} = N_h t_{den,h} + N_h^2 t_{vel,h} + 2 N_d N_h t_{cor,h} + N_d t_{den,d} + N_d^2 t_{vel,d}$$

N_h	$t_{den,h}$ [10^{-5} s]	$t_{vel,h}$ [10^{-5} s]	$t_{cor,h}$ [10^{-5} s]	N_d	$t_{den,d}$ [10^{-5} s]	$t_{vel,d}$ [10^{-5} s]	CPU [seconds]	
							True	Computed
$5 \cdot 10^3$	12.4	(0.120)	0.096	$5 \cdot 10^3$	27.2	0.368	172.0	110.4
10^4	12.4	0.115	0.092	$5 \cdot 10^3$	27.2	0.368	301.6	247.6
10^4			0.096	10^4	27.3	0.222	532.9	437.9
10^4			0.106	$2 \cdot 10^4$	27.4	0.159	1181.7	968.5
10^4	12.4	0.115	0.107	$5 \cdot 10^4$	27.3	0.112	3999.9	3760.5
$2 \cdot 10^4$	12.5	0.108	—	10^5	26.8	0.102	10661.3	10453.0
$2 \cdot 10^4$	12.5	0.108					434.5	426.5
$5 \cdot 10^4$	12.4	0.107					2681.2	2656.9
∞	12.4	0.106	0.114	∞	26.5	0.100		

Table 2

Benchmarks of the code BUILDGAL for (a) spherical halo + disc and (b) axisymmetric halo + disc models. Notation refers to (2); $t_{cor,d} = t_{cor,h}$ by symmetry and has been omitted in the table. We computed CPU values from (2) using the asymptotic limits shown in bold face; true CPU corresponds to clocked time.

$$\text{Total cpu} = N_h t_{den,h} + N_h t_{vel,h} + N_h t_{cor,h} + N_d t_{den,d} + N_d^2 t_{vel,d} + N_d t_{cor,d}$$

N_h	$t_{den,h}$ [10^{-5} s]	$t_{vel,h}$ [10^{-5} s]	$t_{cor,h}$ [10^{-5} s]	N_d	$t_{den,d}$ [10^{-5} s]	$t_{vel,d}$ [10^{-5} s]	$t_{cor,d}$ [10^{-5} s]	CPU [seconds]	
								True	Computed
$5 \cdot 10^3$	3.60	9.40	1.10	$5 \cdot 10^3$	13.4	0.137	1.80	35.7	20.2
10^4	3.80	6.90	1.20	$5 \cdot 10^3$				36.2	20.7
$5 \cdot 10^4$	3.80	4.80	1.30	$5 \cdot 10^3$				40.0	24.5
10^5	3.80	4.60	1.40	$5 \cdot 10^3$	13.4	0.137	1.80	44.8	29.3
$4 \cdot 10^5$	3.70	4.20	1.60					38.0	38.2
$5 \cdot 10^3$	3.60	9.40	1.10	10^4	13.4	0.106	1.80	108.2	78.0
10^4	3.80	6.90	1.20	10^4	13.3	0.110	1.80	108.7	78.5
$5 \cdot 10^4$	3.80	4.80	1.30	10^4	13.1	0.104	1.80	112.5	82.3
10^5	3.80	4.60	1.40	10^4	13.3	0.105	1.80	117.3	87.1
$4 \cdot 10^5$	3.70	4.20	1.60	10^4	13.3	0.105	1.70	145.5	115.7
10^4	3.80	6.90	1.20	$2 \cdot 10^4$	13.3	0.091	1.80	368.2	308.0
$5 \cdot 10^4$	3.80	4.80	1.30	$2 \cdot 10^4$	13.2	0.091	1.80	372.0	311.8
∞	3.72	4.21	1.61	∞	13.3	0.076	1.80		

Table 3

Benchmarks of the new code MAGALIE for spherical or axisymmetric halo + disc models. Notation refers to (2).

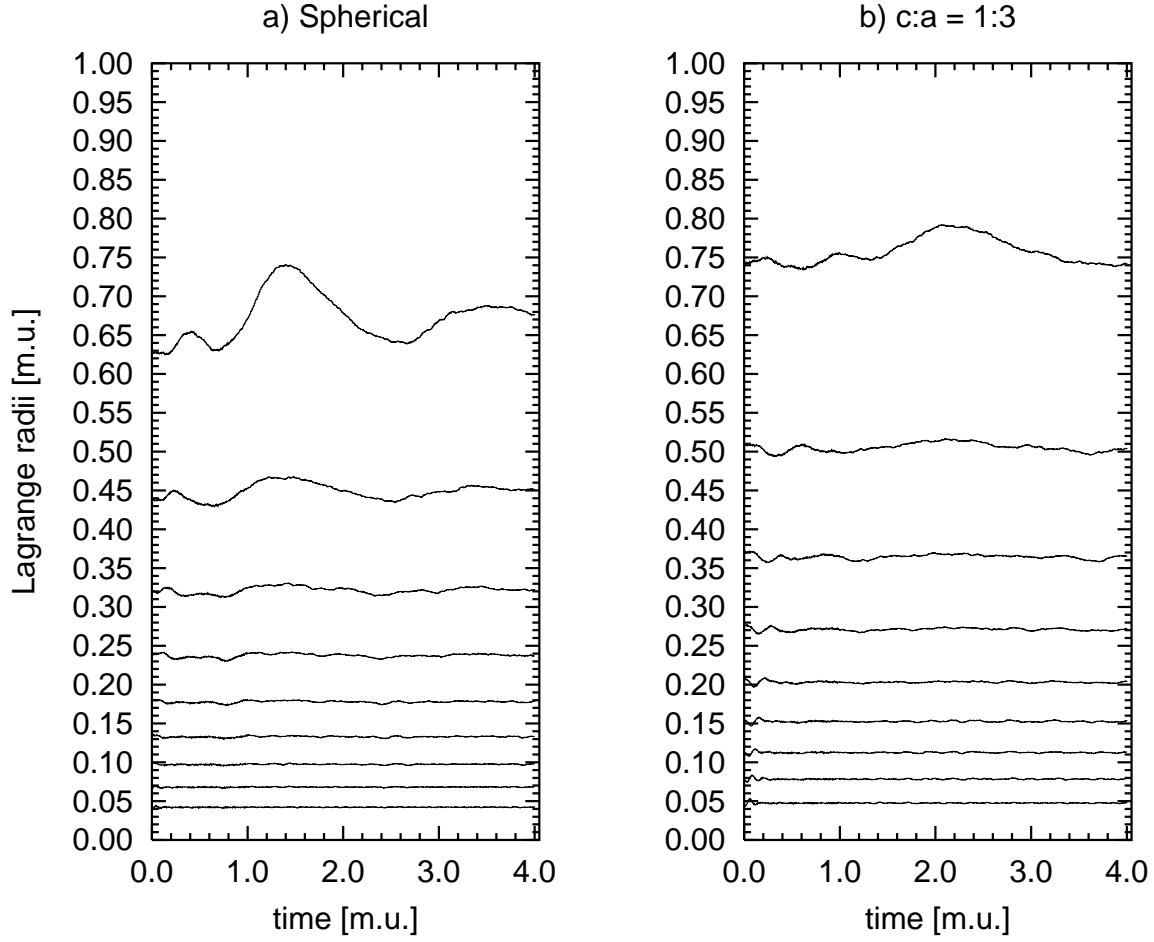


Fig. 2. (a) Evolution of a spherical Dehnen $\gamma = 1$ model. (b) Same model, but flattened to achieve an aspect ratio = 1 : 3. The 10-percentile Lagrange radii are displayed versus time, where one unit of time corresponds to a full revolution at half-mass.

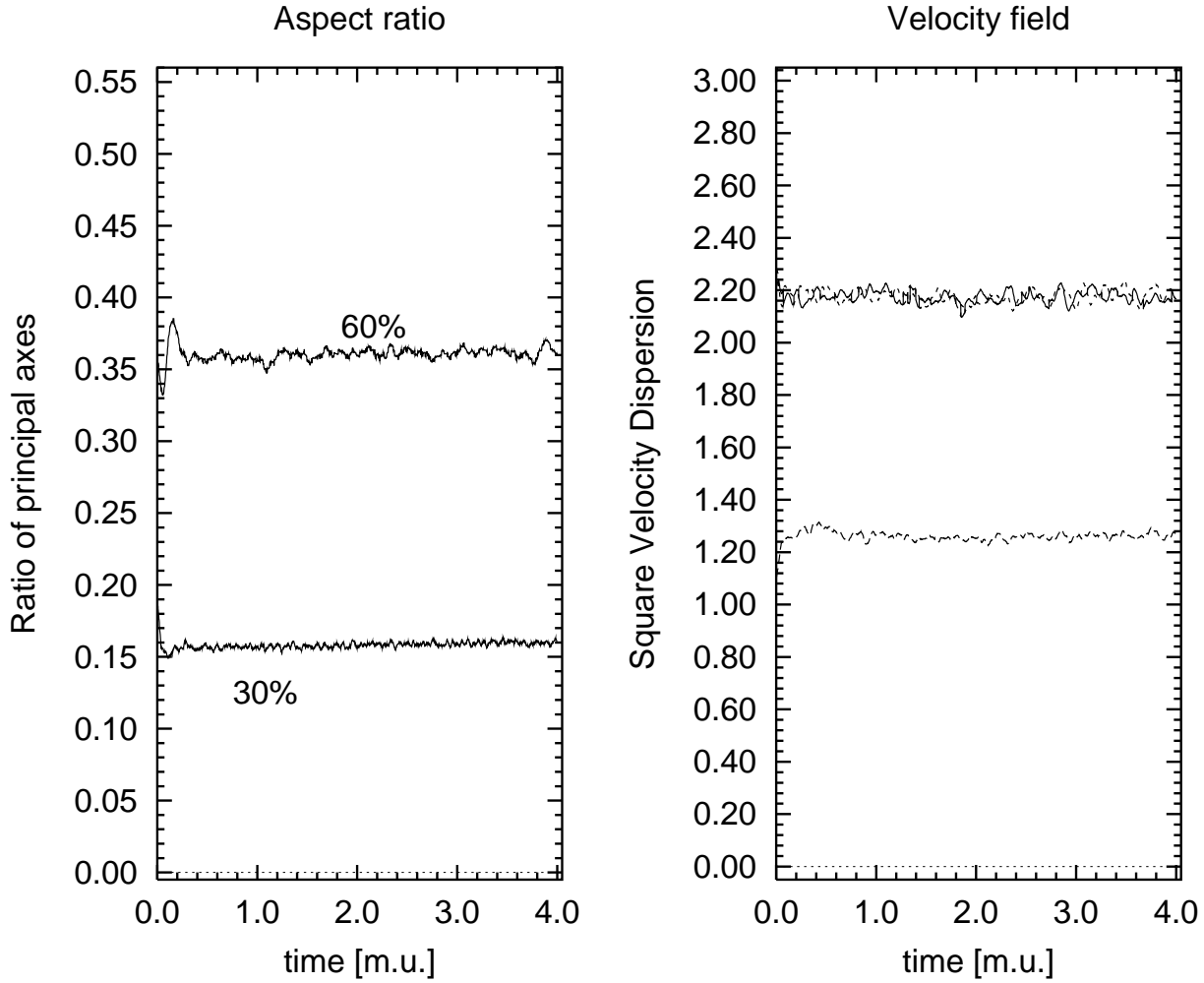


Fig. 3. Left panel: structural evolution of a flattened 1:3 Dehnen $\gamma = 1$ model. The ratio of minor to major axes are computed at two different Lagrange radii enclosing 30% or 60% of the total mass. Note: the results at 30% Lagrange radius were divided by two to avoid overlap with the others. Right panel: components of the velocity dispersion tensor (cf. Eq. 21) for the innermost 60% particles. The lower curve is the z-component. The velocity dispersions were computed along the eigenvectors of the rotational inertia tensor.

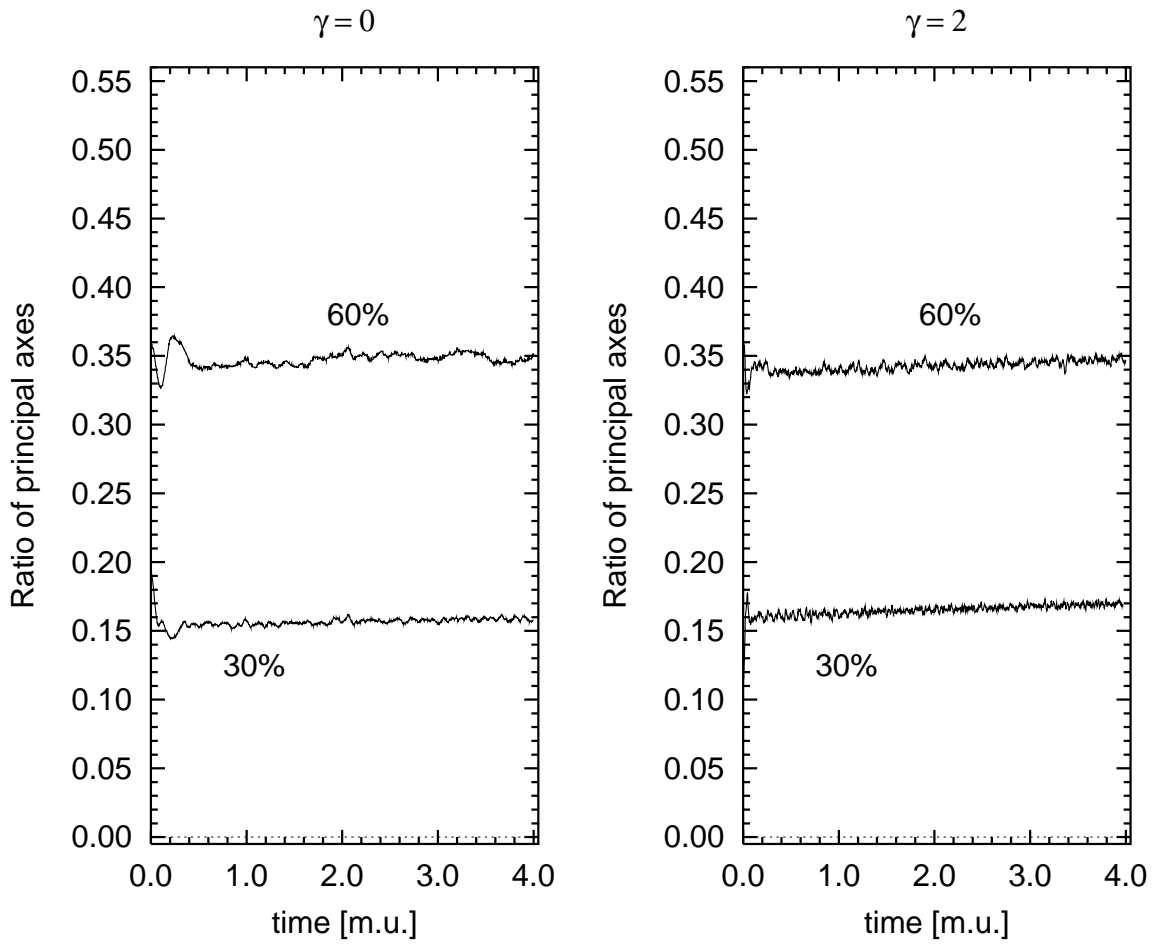


Fig. 4. As for Fig.3. Time evolution of two flattened Dehnen models of aspect ratio 1:3, with $\gamma = 0$ (left) and $\gamma = 2$ (right). The principal axes (21) were computed at the 30% and 60% spherical Lagrange radii. The 30%-results were divided by two to distinguish the two curves on each panels.

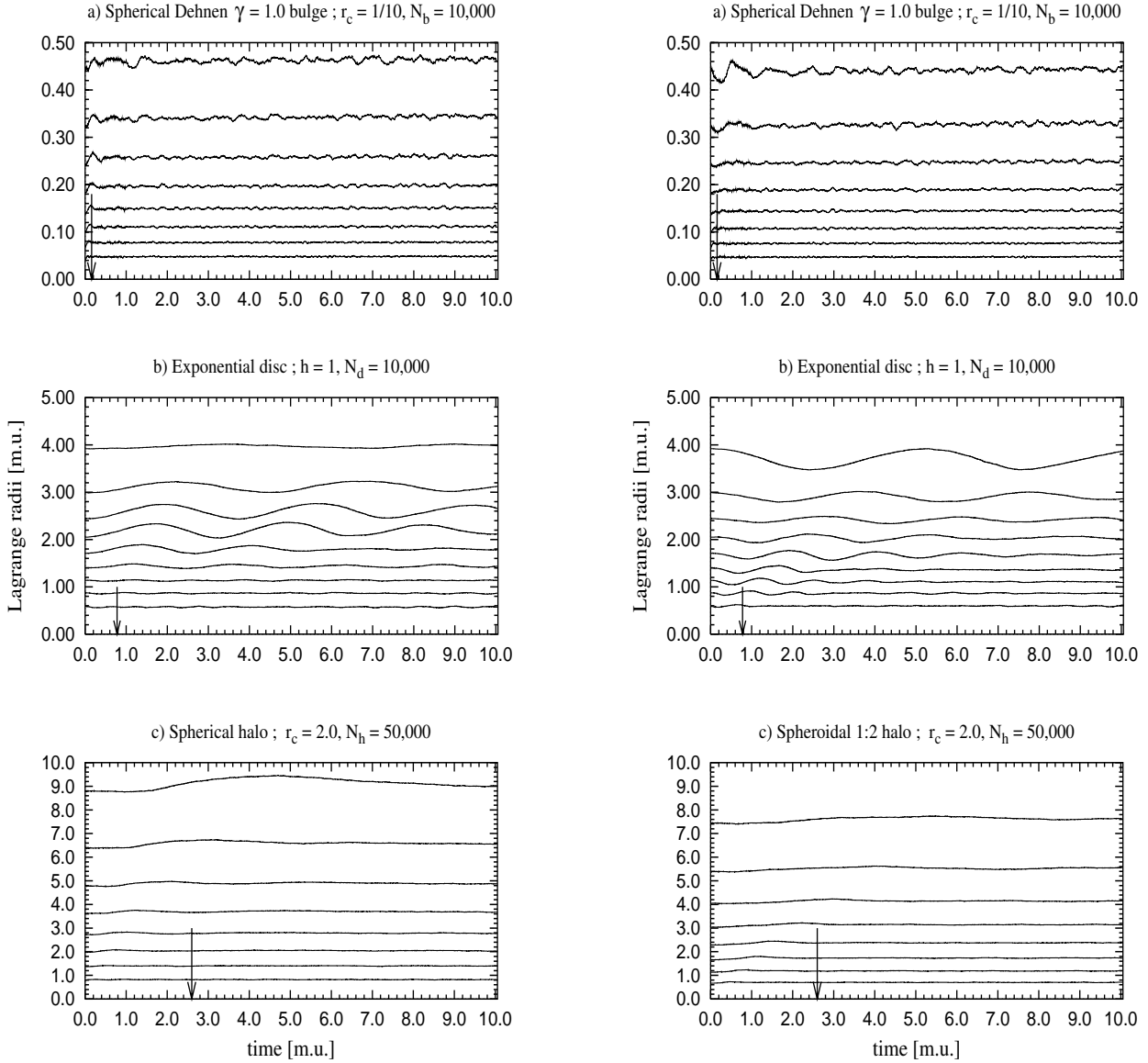


Fig. 5. Left panels: evolution of the Lagrange radii (including 10, 20, 30 ... percent of the component's mass) for a three-component model with spherical bulge and halo. Right panels: as on the left, but with a spheroidal halo of aspect ratio 1:2. The arrows indicate the circular period at the 50% Lagrange radius (bulge and halo) and at the radial scale length h (disc, middle panel).

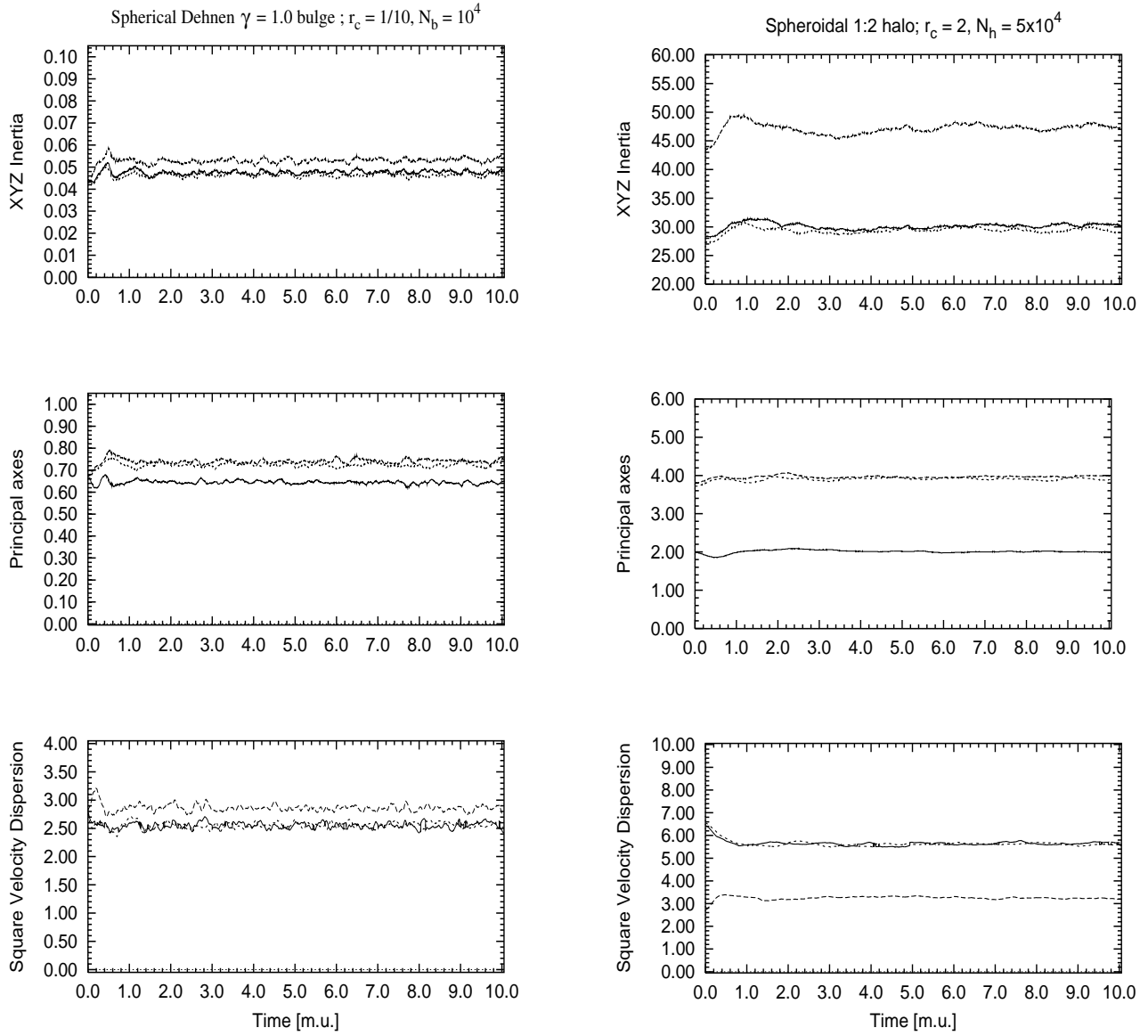


Fig. 6. Time-evolution of the morphology of individual components. Left-hand panels: central bulge parameters; right-hand panels: halo parameters. The quantities were measured at the 50% spherical Lagrange radius. The principal axes were computed as in (Fig. 3). The XYZ Inertia are the eigenvalues of the rotational inertia tensor (Goldstein 1980).